第 30 卷 第 8 期 催 化 学 报 2009 年 8 月
Vol. 30 No. 8 *Chinese Journal of Catalysis* August 2009

文章编号: 0253-9837(2009)08-0839-13 **综述:** 839~851

二氧化钛纳米材料及其能源应用

陈晓波

劳伦斯伯克利国家实验室, 伯克利, 加利福尼亚 94720, 美国

摘要: 简要介绍了二氧化钛纳米材料的合成、性质、改性及其在能源方面的应用. 其中合成方法包括溶胶凝胶、水/溶剂热、氧化、沉积和超声/微波助合成法; 性质包括结构和热力学以及电学和光学性质; 改性包括掺杂和敏化; 应用包括光催化、光伏打和光解水.

关键词: 二氧化钛; 纳米材料; 掺杂; 敏化; 光催化; 光伏打; 光解水

中图分类号: O643 **文献标识码:** A

Titanium Dioxide Nanomaterials and Their Energy Applications

CHEN Xiaobo*

Lawrence Berkeley National Laboratory, Berkeley, California 94720, USA

Abstract: Here we briefly introduce the synthesis, properties, modifications, and energy applications of titanium dioxide nanomaterials. This introduction surveys their synthetic methods (sol/sol-gel, hydro/solvo-thermal, oxidation, deposition, sonochemical, and microwave-assisted approaches), their structural and thermodynamic properties, their modifications (doping and sensitizing), and their applications in photocatalysis, photovoltaics and solar water splitting.

Key words: titanium dioxide; nanomaterial; doping; sensitizing; photocatalysis; photovoltaics; solar water splitting

Titanium dioxide (TiO_2) is biocompatible and environmentally benign and has been widely used as a pigment [1–3]. Manufacture of titanium dioxide pigment is a combination of two distinct processes: base pigment particle production and surface treatment, drying and milling. There are two different process routes used to extract and purify TiO_2 from ore to produce core pigment particles: the sulfate process and the chloride process [4].

The sulfate process is the first commercial process for the manufacture of TiO_2. Originally ilmenite is used as a raw material, but beneficiated ores with a much higher TiO_2 assay have been used more recently. The ore is first dried, ground, and classified to ensure efficient sulfation by agitation with concentrated sulfuric acid. The resultant metal sulfates are dissolved in water or weak acid, and the solution is treated to ensure that only ferrous-state iron is present. The solution temperature is reduced to avoid premature hydrolysis and clarified by settling and chemical flocculation. The clear solution is then further cooled to crystallize coarse ferrous sulfate heptahydrate ($FeSO_4·7H_2O$) which is separated from the process. The solution is evaporated to a precise composition and hydrolyzed to produce a suspension consisting predominantly of clusters of colloidal hydrous titanium oxide. Precipitation is carefully controlled to achieve the necessary particle size, usually employing a seeding or nucleating technique. The suspension is then separated from the mother liquor and extensively washed to remove residual traces of metallic impurities, using chelating agents if necessary. The washed suspension is treated with chemicals which adjust the physical texture and act as catalysts in the calcination step. This process can produce either anatase or rutile crystal forms depending on additives used prior to calcination.

The feedstock for the chloride process is a mineral rutile or synthetic beneficiates containing over 90 percent TiO_2. A suitable ore blend is mixed with a source of carbon and then reacted with chlorine at approximately 900 °C. The reaction yields titanium tetrachloride, $TiCl_4$, and the chlorides of all the impurities present. The mixed chlorides are cooled and the low-volatile chloride impurities (e.g. iron, manganese,

Received date: 29 April 2009.

***Corresponding author.** Tel: +1-510-486-7140; Fax: +1-510-486-7303; E-mail: XChen3@lbl.gov

English edition available online at ScienceDirect (http://www.sciencedirect.com/science/journal/18722067).

and chromium) are separated by condensation and removed from the gas stream with any unreacted solid starting materials. The $TiCl_4$ vapor is condensed to a liquid, followed by fractional distillation to produce an extremely pure, colorless, mobile liquid $TiCl_4$ intermediate product, freezing at –24 °C and boiling at 136 °C. The second critical stage in the chloride process is oxidation of the $TiCl_4$ to TiO_2 pigment particles. Pure titanium tetrachloride is reacted with oxygen in an exothermic reaction to form titanium dioxide and liberate chlorine, which is recycled to the chlorination stage. The high temperature ensures that only the rutile crystal form is produced. After cooling, the gas stream passes through a separator to collect the pigment particles and to remove adsorbed chlorine from the pigment. In both processes, the raw pigment may either be dried, milled, packed, and sold or more likely, especially for rutile pigments, surface-treated to produce a range of special products for various applications.

Recent enormous research efforts dedicated to TiO_2 materials have been most fascinated with the discovery of the phenomenon of photocatalytic splitting of water on a TiO_2 electrode by Fujishima et al. in 1972 [5–7]. An exponential growth of research activities has been seen in nanoscience and nanotechnology in the past decades [8–15]. TiO_2 nanomaterials, including nanoparticles, nanorods, nanowires, and nanotubes, are widely investigated for various applications in photocatalysis, photovoltaics, batteries, photonic crystals, sensors, ultraviolet blockers, smart surface coatings, pigment, and paints [1–24]. Various methods, such as sol-gel, sol, hydrothermal/solvothermal, physical/chemical vapor deposition, electrodeposition, etc., have been successfully used in making TiO_2 nanomaterials. In the nanometer scale, new physical and chemical properties emerge and they vary with the sizes and shapes of the nanomaterials. The movement of electrons and holes in semiconductor nanomaterials is governed by the well-known quantum confinement, the transport properties related to phonons and photons are largely affected by the size and geometry of the materials, and the specific surface area and surface-to-volume ratio increase dramatically as the size of a material decreases [8–13]. The high surface area brought about by small particle size is beneficial to most TiO_2-based devices, as it facilitates reaction/interaction between the devices and interacting media, which mainly occurs on the surface and depends on the surface area. As the size, shape, and crystal structure of TiO_2 nanomaterials change, not only does surface stability vary, but the transitions between different phases of TiO_2 under pressure or heat become size dependent as well.

1 Preparation methods

1.1 Sol/sol-gel methods

TiO_2 nanomaterials have been synthesized with the sol-gel method, a widely used method in making various ceramic materials. In a typical sol-gel process, the hydrolysis of a titanium alkoxide or halide precursor and subsequent condensation finally lead to the formation of TiO_2 inorganic framework. This process normally proceeds via an acid-catalyzed hydrolysis step of titanium (IV) alkoxide followed by condensation [25–27]. The development of Ti–O–Ti chains through alcoxolation is favored for low content of water, with low hydrolysis rates and excess titanium alkoxide in the reaction mixture. Three-dimensional polymeric skeletons with close packing are resulted from the development of Ti–O–Ti chains, since each Ti is coordinated with four O atoms. The formation of $Ti(OH)_4$ is favored with high hydrolysis rates. The presence of a large quantity of Ti–OH and insufficient development of three-dimensional polymeric skeletons lead to loosely packed first-order particles. The formation of $Ti(OH)_4O^+H_2$ by the coordination of water to $Ti(OH)_4$ is favored in the presence of a large excess of water. Closely packed first-order particles are yielded via a three-dimensionally developed gel skeleton. Ti–O–Ti chains are formed in the reactions of the formed Ti–O^+H–H species with other Ti–OH with the production of water or alcohol. The rate constant for coarsening increased with temperature due to the temperature dependence of the viscosity of the solution and the equilibrium solubility of TiO_2. Secondary particles were formed by epitaxial self-assembly of primary particles at longer times and higher temperatures, and the number of primary particles per secondary particle increased with time. The average TiO_2 nanoparticle radius increased linearly with time in agreement with the Lifshitz-Slyozov-Wagner model for coarsening [26].

The sol method here refers to the non-hydrolytic sol-gel processes and usually involves the reaction of titanium chloride with a variety of different oxygen donor molecules, e.g. a metal alkoxide or an organic ether [28–36]. The condensation between Ti–Cl and Ti–OR leads to the formation of Ti–O–Ti bridges. The alkoxide groups can be provided by titanium alkoxides or can be formed in situ by reaction of the titanium chloride with alcohols or ethers. For a series of alkyl substituents including methyl, ethyl, isopropyl, and tert-butyl, the reaction rate dramatically increased with greater branching of R, while average particle sizes were relatively unaffected. Variation of R yielded a clear trend in average particle size, but without discernible trend in reaction rate. Increasing nucleophilicity (or size) of the halide resulted in smaller anatase crystals. Average sizes ranged from 9.2 nm for TiF_4 to 3.8 nm for TiI_4. The amount of passivating agent influenced the chemistry [36].

Micelles and inverse micelles are commonly employed to synthesize TiO_2 nanoparticles in the sol and sol-gel methods

[37–42]. In micelles, the hydrophobic hydrocarbon chains of the surfactants are oriented toward the interior of the micelle, and the hydrophilic groups of the surfactants are towards with the surrounding aqueous medium. Reverse micelles are formed in nonaqueous media and the hydrophilic headgroups are directed toward the core of the micelles while the hydrophobic groups are directed outward. Micelles are often globular and roughly spherical in shape, but ellipsoids, cylinders, and bilayers are also possible. The shape of a micelle is a function of the molecular geometry of its surfactant molecules and solution conditions such as surfactant concentration, temperature, pH, and ionic strength. The TiO_2 nanoparticles prepared with the above micelle and reverse micelle methods normally have amorphous structure, and calcination is usually necessary in order to induce high crystallinity. However, this process usually leads to the growth and agglomeration of TiO_2 nanoparticles. The crystallinity of TiO_2 nanoparticles initially (synthesized by controlled hydrolysis of titanium alkoxide in reverse micelles in a hydrocarbon solvent) could be improved by annealing in the presence of the micelles at temperatures considerably lower than those required for the traditional calcination treatment in the solid state [40]. This procedure resulted in crystalline TiO_2 nanoparticles with unchanged physical dimensions and minimal agglomeration [40].

Surfactants have been widely used in the preparation of variety of nanoparticles with good size distribution and dispersity [43–50]. Adding different surfactants as capping agents such as acetic acid and acetylacetone into the reaction matrix can help synthesize monodispersed TiO_2 nanoparticles [43,44]. With the aid of surfactants, different sized and shaped TiO_2 nanorods have been synthesized [46,47]. The growth of high aspect ratio anatase TiO_2 nanorods could be achieved by controlled hydrolysis of titanium tetraisopropoxide (TTIP) in oleic acid (OA). A kinetically overdriven growth mechanism led to the growth of TiO_2 nanorods instead of nanoparticles [46]. The shape of TiO_2 nanocrystals could be modified by changing the surfactant concentration. For example, at low lauric acid concentrations, bullet- and diamond-shaped nanocrystals were obtained; at higher concentrations, rod-shaped nanocrystals or a mixture of nanorods and branched nanorods were observed [49].

Ordered TiO_2 nanorods, nanowire, and nanotube arrays TiO_2 can be obtained by combining the sol-gel method with an anodic alumina membrane (AAM) template by dipping porous AAMs into boiled TiO_2 sol followed by drying and heating processes [51], by sol-gel electrophoretic deposition of TiO_2 colloidal suspensions into AAM [52], or using the sol-gel method by templating with AAM [53] and other organic compounds [54].

1.2 Hydro/solvo-thermal methods

The hydrothermal method has been widely used to prepare TiO_2 nanomaterials [55–67]. Hydro/solvo-thermal synthesis is normally conducted in steel pressure vessels called autoclaves under controlled temperature and/or pressure with the reaction in aqueous/organic solutions. The temperature can be elevated above the boiling point of the water/organics, reaching the pressure of vapor saturation. The temperature and the amount of solution added to the autoclave largely determine the internal pressure produced. The solvothermal method is almost identical to hydrothermal method except that the solvent used here is non-aqueous. However, the temperature can be elevated much higher than that in hydrothermal method because a variety of organic solvent with high boiling points can be chosen. The solvothermal method normally has better control than hydrothermal methods of the size, shape distributions, and the crystallinity of TiO_2 nanoparticles. For example, by hydrothermal treatment of a titanium trichloride aqueous solution supersaturated with NaCl at 160 ºC for 2 h, TiO_2 nanorods could be prepared [57]. Different surfactants or compositions can be used to tune the morphology of the resulting nanorods [58,59]. When TiO_2 powders are put into a 2.5–20 mol/L NaOH aqueous solution and held at 20–110 °C for 20 h in an autoclave, TiO_2 nanotubes are obtained [62,63]. With/without the aid of surfactants, the solvothermal method has been employed to synthesize high-quality TiO_2 nanoparticles and nanorods [64–67]. For example, narrow-dispersed TiO_2 nanorods could be obtained by keeping TTIP dissolved in anhydrous toluene with OA as a surfactant at 250 ºC for 20 h in an autoclave [66].

1.3 Oxidation methods

By oxidation of titanium metal using oxidants or under anodization, TiO_2 nanomaterials can be obtained. TiO_2 nanotubes by electrochemical oxidation of titanium foil has been extensively studied [68–73]. For example, by anodizing titanium sheet under 10–20 V in a 0.5% hydrogen fluoride electrolyte solution for 10–30 min, aligned TiO_2 nanotube arrays can be obtained. The length and diameter of the TiO_2 nanotubes could be controlled over a wide range (diameter, 15–120 nm; length, 20 nm to 10 μm) with the applied potential between 1 and 25 V in optimized phosphate/HF electrolytes. Crystallized TiO_2 nanotubes were obtained after the anodized titanium plate was annealed at 500 °C for 6 h in oxygen [70]. This method normally produces large TiO_2 nanotubes with diameters over 50 nm. Figure 1 shows typicl SEM and TEM images of TiO_2 nanotubes we fabricated by this method with HCl as etching acid [73].

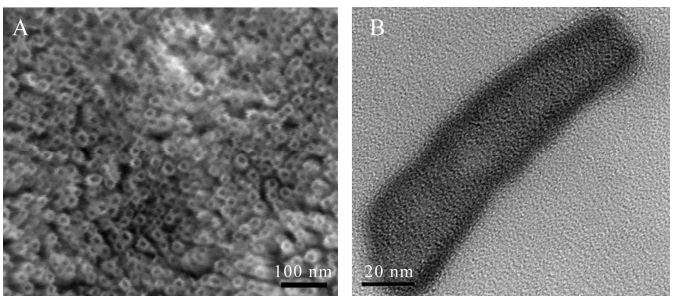


Fig. 1. SEM (A) and TEM (B) images of TiO_2 nanotubes fabricated by the electroxidation method [73].

Direct oxidation of a titanium metal plate with hydrogen peroxide can lead to the formation of TiO_2 nanorods [74,75]. By the addition of inorganic salts of NaX (X = F^-, Cl^-, and SO_4^{2-}), the crystalline phase of TiO_2 nanorods were controlled. The addition of F^- and SO_4^{2-} helped the formation of pure anatase, while the addition of Cl^- favored the formation of rutile. The anions affected the precipitation rate [74].

Aligned TiO_2 nanorod arrays were obtained by oxidizing titanium substrate using acetone as the oxygen source at 850 ºC for 90 min [76]. The oxygen source was found to play an important role. Highly dense and well-aligned TiO_2 nanorod arrays were formed when acetone was used as the oxygen source. Crystal-grain films were obtained with pure oxygen, and random nanofibers growing from the ledges of the TiO_2 grains were produced with argon mixed with a low concentration of oxygen. Large polycrystalline TiO_2 grains were formed with pure oxygen, since oxygen diffusion predominated because of the high oxygen concentration and the oxidation occurred at the Ti metal and the TiO_2 interface. When acetone was used as the oxygen source, well aligned TiO_2 nanorod arrays were formed when Ti cations diffused to the oxide surface and reacted with the adsorbed acetone species.

1.4 Deposition methods

Vapor deposition refers to any process in which materials in a vapor state are condensed to form a solid phase material. Vapor deposition processes usually take place within a vacuum chamber. If no chemical reaction occurs, this process is called physical vapor deposition (PVD), otherwise it is called chemical vapor deposition (CVD). In CVD processes, thermal energy heats the gases in the coating chamber and drives the deposition reaction. Other CVD approaches include electrostatic spray hydrolysis, diffusion flame pyrolysis, thermal plasma pyrolysis, ultrasonic spray pyrolysis, laser-induced pyrolysis, and ultronsic-assisted hydrolysis. In PVD, materials are first evaporated and then condensed to form a solid material. The primary PVD methods include thermal deposition, ion plating, ion implantation, sputtering, laser vaporization, and laser surface alloying.

Thick crystalline TiO_2 films with grain sizes below 30 nm as well as TiO_2 nanoparticles with sizes below 10 nm were prepared by pyrolysis of TTIP in a mixed helium/oxygen atmosphere, using liquid precursor delivery [77]. In another example, TiO_2 nanorods were developed grown on fused silica substrates with a template- and catalyst-free metalorganic CVD (MOCVD) method [78]. Titanium acetylacetonate ($Ti(C_{10}H_{14}O_5)$) placed on a Pyrex glass container was used as the precursor. The precursor was loaded into the low-temperature zone of a furnace at 200–230 °C to vaporize. The vapor was carried by a N_2/O_2 flow into the high-temperature zone of the furnace, and TiO_2 nanostructures were grown directly on bare fused silica or silicon substrates at 500–700 °C. The final crystalline phase and morphology were dependent on the reaction conditions. At 630 and 560 °C under a pressure of 5 Torr, single-crystalline rutile and anatase TiO_2 nanorods were formed respectively; while at 535 °C under 3.6 Torr, anatase TiO_2 nanowalls composed of well-aligned nanorods were formed.

TiO_2 nanowire arrays have been fabricated by a simple PVD method or thermal deposition [79–81]. Typically, pure Ti metal powder was loaded as the titanium source on a quartz boat in a tube furnace. The substrate was kept ~0.5 mm away from the source. The temperature was increased to 850 °C under an argon gas flow protection. Then the furnace chamber was pumped down to ~300 Torr and the flow rate of the argon gas was set at 100 sccm (standard cubic centimeter per minute) and held for 3 h. After the reaction, a layer of TiO_2 nanowires was obtained [79]. Alternatively, a layer of Ti nanopowders can be deposited on the substrate before the growth of TiO_2 nanowires [80,81], and Au can be employed as catalyst [80].

1.5 Sonochemical and microwave-assisted methods

The sonochemical method has been applied to prepare various TiO_2 nanomaterials by different groups [41,82–85]. Sonochemistry arises from acoustic cavitation: the formation, growth, and implosive collapse of bubbles in a liquid. Cavitational collapse produces intense local heating (~5 000

K), high pressures (~1 000 atm), and enormous heating and cooling rates (>10^9 K/s). Highly photoactive TiO_2 nanoparticle photocatalysts with anatase and brookite phases can be obtained using the hydrolysis of titanium tetraisoproproxide in pure water or in a 1:1 EtOH-H_2O solution under ultrasonic radiation [41]. Arrays of TiO_2 nanowhiskers with a diameter of 5 nm and nanotubes with a diameter of ~5 nm, and a length of 200–300 nm could be obtained by sonicating TiO_2 particles in NaOH aqueous solution followed by washing with deionized water and dilute HNO_3 aqueous solution [85].

Microwave radiation is applied to prepare various TiO_2 nanomaterials [86–88]. A dielectric material can be processed with energy in the form of high-frequency electromagnetic waves. The principal frequencies of microwave heating are between 900 and 2 450 MHz. At lower microwave frequencies, conductive currents flowing within the material due to the movement of ionic constituents can transfer energy from the microwave field to the material. At higher frequencies, the energy absorption is primarily due to molecules with permanent dipole, which tend to re-orientate under the influence of a microwave electric field. This re-orientation loss mechanism originates from the inability of the polarisation to follow extremely rapid reversals of the electric field, so the polarisation phasor lags the applied electric field. This ensures that the resulting current density has a component in phase with the field, and therefore power is dissipated in the dielectric material. The major advantages of using microwaves for industrial processing are rapid heat transfer and volumetric and selective heating. Colloidal titania nanoparticle suspensions could be prepared within 5 to 60 min with microwave radiation, while 1 to 32 h was needed for the conventional synthesis method of forced hydrolysis at 195 °C [86]. TiO_2 nanotubes can be synthesized with microwave radiation via the reaction of TiO_2 crystals of anatase, rutile, or mixed phase and NaOH aqueous solution under certain microwave power [88]. Normally, the TiO_2 nanotubes had the central hollow, open-ended and multi-wall structure with diameters of 8–12 nm and lengths up to 200–1000 nm [88].

2 Properties

2.1 Structural and thermodynamic properties

TiO_2 has three phases of crystal structures, namely anatase, rutile, and brookite. The most commonly seen phases are anatase and rutile. For the bulk TiO_2 material, rutile is the stable phase at high temperatures, but anatase and brookite are common in fine grained (nano-scale) natural and synthetic samples. On heating concomitant with coarsening, the following transformations are all seen: anatase to brookite to rutile, brookite to anatase to rutile, anatase to rutile, and brookite to rutile. These transformation sequences imply very closely balanced energetics as a function of particle size. The surface enthalpies of the three polymorphs are sufficiently different that crossover in thermodynamic stability can occur under conditions that preclude coarsening, with anatase and/or brookite stable at small particle size [89,90]. In reality, the crystal structure of TiO_2 nanoparticles depended largely on the preparation method [91]. For small TiO_2 nanoparticles (< 50 nm), anatase seemed more stable and transformed to rutile at > 973 K. In another study, the prepared TiO_2 nanoparticles had anatase and/or brookite structures, which transformed to rutile after reaching a certain particle size [89,92]. Once rutile was formed, it grew much faster than anatase. When the particle size was larger than 14 nm, rutile became more stable than anatase. A slow phase transition was observed from brookite to anatase below 1 053 K along with grain growth, a rapid brookite to anatase and anatase to rutile transformations between 1 053 K and 1 123 K, and rapid grain growth of rutile above 1 123 K as the dominant phase [93].

Surface passivation had an important impact on nanocrystal morphology and phase stability [94–96]. The surface hydrogenation induced significant changes in the shape of rutile nanocrystals, but not in anatase, and that the size at which the phase transition might be expected increased dramatically when the under-coordinated surface titanium atoms were H-terminated. For example, for spherical particles, the cross-over point was about 2.6 nm. For clean and faceted surface, at low temperatures, a phase transition pointed at an average diameter of approximately 9.3–9.4 nm for anatase nanocrystals, the transition size decreased slightly to 8.9 nm when the surface bridging oxygens were H-terminated, and increased significantly to 23.1 nm when both the bridging oxygens and under-coordinated titanium atoms of the surface trilayer were H-terminated. Below the cross point, anatase phase was more stable than rutile phase [94].

2.2 Electronic and optical properties

The electronic structure of TiO_2 has been studied by various experimental techniques, i.e. X-ray photoelectron, X-ray absorption and emission spectroscopies [91,97,98]. It is well known that for nanoparticles the bandgap energy increases and the energy band becomes more discrete with decreasing size [99,100]. As the size of a semiconductor nanoparticle falls below the Bohr radius of the first excitation state or comparable to the DeBroglie wavelength of the charge carriers, the charge carriers begin to behave quantum mechanically and the charge confinement leads to a series

of discrete electronic states [101]. However, there is discrepancy on this critical size, below which quantization effects are observed for TiO_2 nanomaterials with indirect bandgaps. The estimated critical diameter depends critically on the effective masses of the charge carriers [102]. The excitation radii for titania particles was found between 0.75 and 1.9 nm in two studies [103,104].

The main mechanism of light absorption in pure semiconductors is direct interband electron transitions. This absorption is especially small in indirect semiconductors, e.g. TiO_2, where the direct electron transitions between the band centers are prohibited by the crystal symmetry. Indirect electron transitions with momentum nonconservation at the interface can enhance the light absorption in small TiO_2 crystallites [105]. This effect increases at a rough interface when the share of the interface atoms is larger. The indirect transitions are allowed due to a large dipole matrix element and a large density of states for the electron in the valence band. Considerable enhancement of the absorption is expected in small TiO_2 nanocrystals, as well as in porous and microcrystalline semiconductors, when the share of the interface atoms is sufficiently large. A rapid increase in the absorption takes place at low ($h\nu < E_g + W_c$, W_c: width of conduction band) photon energies. Electron transitions to any point in the conduction band become possible when $h\nu = E_g + W_c$. Further enhancement of the absorption occurs due to an increase of the electron density of states in only the valence band. The interface absorption becomes the main mechanism of light absorption for the crystallites that are smaller than 20 nm [105]. Due to lower dimensionality, the band gap of TiO_2 nanomaterials was larger than the band gap of bulk TiO_2 [106,107].

3 Modifications

Many applications of TiO_2 nanomaterials are closely related to their optical properties. However, the highly efficient use of TiO_2 nanomaterials is sometimes prevented by the wide bandgap of TiO_2. The bandgap of bulk TiO_2 lies in the UV regime (3.0 eV for rutile phase and 3.2 eV for anatase phase), which is only a small fraction of the sun's energy (< 10%) [24]. Thus, one of the goals for improvement of the performance of TiO_2 nanomaterials is to increase their optical activity by shifting the onset of the response from the UV to the visible region [9]. There are several ways to achieve this goal. First, doping TiO_2 nanomaterials with other elements can narrow the electronic properties and thus alter the optical properties of TiO_2 nanomaterials. Second, sensitizing TiO_2 with other colorful inorganic or organic compounds can improve its optical activity in the visible light region. Third, coupling collective oscillations of the electrons in the conduction band of metal nanoparticle surfaces to those in the conduction band of TiO_2 nanomaterials in metal-TiO_2 nanocomposites can improve the performance. In addition, the modification of TiO_2 nanomaterials surface with other semiconductors can alter the charge transfer properties between TiO_2 and the surrounding environment, thus improving the performance of TiO_2 nanomaterials based devices. Figure 2 illustrates the modification paths in improving the properties (mainly the optical properties) of TiO_2 nanomaterials.

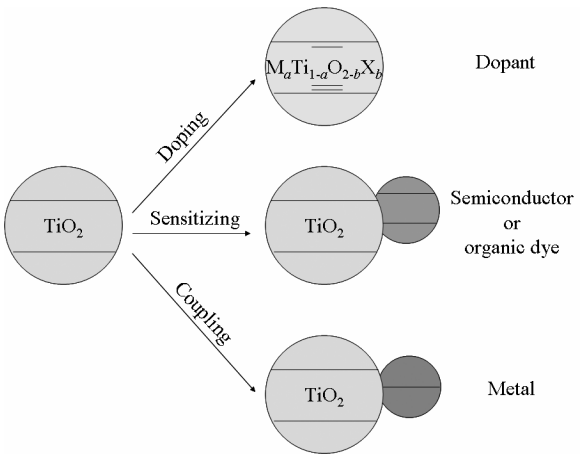


Fig. 2. Illustration of the modification paths for TiO_2 nanomaterials.

3.1 Doping

A variety of metal and nonmetal elements have been doped into TiO_2 nanomaterials [108–132]. The preparation methods of doped TiO_2 nanomaterials can be divided into three types: wet chemistry, high temperature treatment, and ion implantation on TiO_2 nanomaterials. The wet chemistry method usually involves hydrolysis of a titanium precursor in a mixture of water and other reagents, followed by heating. TiO_2 nanoparticles were doped with 21 metal ions by the sol-gel method, and the presence of metal ion dopants significantly influenced the photoreactivity, charge carrier recombination rates, and interfacial electron-transfer rates [112]. C-doped TiO_2 nanomateirals have been obtained by heating titanium carbide [114], or by annealing TiO_2 under CO gas flow at high temperatures (500–800 °C) [115], or by direct burning of a titanium metal sheet in a natural gas flame [116]. N-doped TiO_2 nanomaterials have been synthesized by hydrolysis of TTIP in a water/amine mixture and the post-treatment of the TiO_2 sol with amines [108] or directly from a Ti-bipyridine complex [122].

A red shift in the band gap transition or visible-light absorption was observed in metal-doped TiO_2 [112,133,134]. For V-, Mn-, or Fe-doped TiO_2, the absorption spectra shifted to a lower energy region with an increase in the dopant concentration [112,133,134]. This red shift was at-

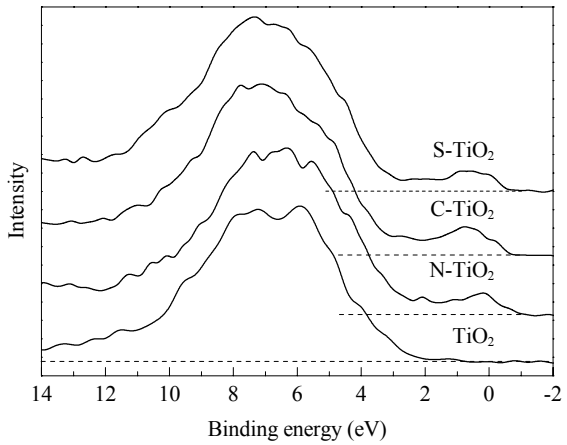


Fig. 3. Valence band (VB) X-ray photoelectron spectroscopy (XPS) spectra of pure rutile TiO_2, N-, C-, and S-doped TiO_2 [136].

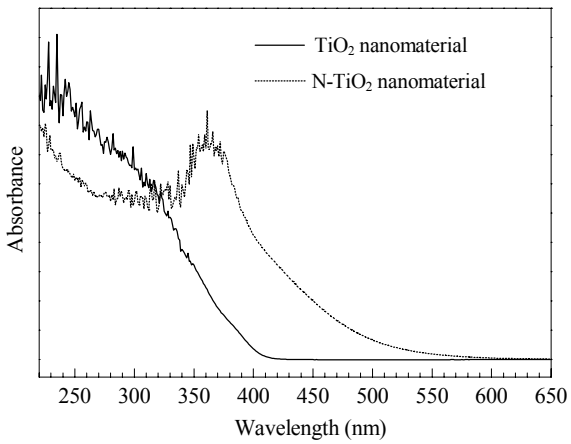


Fig. 4. Absorbance spectra of N-doped TiO_2 nanoparticles and pure TiO_2 nanoparticles.

tributed to the charge-transfer transition between the *d*-electrons of the dopant and the conduction band (or valance band) of TiO_2. Our recent study on the electronic properties of C-, N-, and S-doped TiO_2 has revealed that compared to pure TiO_2, there are more electronic states above the valence band edge of TiO_2 in these doped TiO_2 materials (Fig. 3) using X-ray absorption, emission, and photoelectron spectroscopies [135,136]. This can explain the visible-light absorption properties of the doped TiO_2 materials.

Nonmetal doped TiO_2 normally has color from white to yellow or even light gray, and the onset of absorption spectra red-shifted to longer wavelength [108,110,118,122,125]. In N-doped TiO_2 nanomaterials, the band gap absorption onset shifted 600 nm from 380 nm of the undoped TiO_2, extending the absorption up to 600 nm (Fig. 4). The optical absorption of N-doped TiO_2 in the visible light region was primarily located between 400 and 500 nm, while that of oxygen-deficient TiO_2 was mainly above 500 nm from their density-functional theory study [137]. The red-shift in the absorption spectra of doped TiO_2 is due to the narrowing of the band gap in the electronic structure after doping. This could increase photosensitivity of the materials, i.e. photocatalytic, photochemical, and photoelectrochemical activities, in the visible region.

3.2 Sensitizing

Narrow bandgap semiconductors have been used as sensitizers to improve the optical absorption properties of TiO_2 nanomaterials in the visible light region by various groups [138–140]. In the sensitization of a nanocrystalline TiO_2 matrix by small PbS nanoparticles (< 2.5 nm), the photogenerated excess electrons could be directly injected from the PbS to the TiO_2, resulting in strong photoconductance in the visible region [139]. Excitation of the sensitizer AgI on TiO_2 nanoparticles resulted in a stabilization of electron-hole pairs with a lifetime well beyond 100 μs and in electron migration from AgI to TiO_2 [138]. In the sensitization of nanoporous TiO_2 by CdS, PbS, Ag_2S, Sb_2S_3, and Bi_2S_3, the relative positions of the energetic levels at the interface between the quantum size particles and TiO_2 could be optimized for efficient charge separation by using the size quantization effect, and the photostability of the electrodes could be significantly enhanced by surface modification of the TiO_2 nanoparticles with CdS nanoparticles [140].

When the TiO_2 nanoparticle films were sensitized with Ag nanoparticles, the color of the film could be reversely switched back and forth between brownish-gray under UV light and the color of illuminating visible light due to the oxidation of Ag by O_2 under visible light and reduction of Ag^+ under UV light [141]. The color of the film under visible light could be tuned from green to red and white by changing the size of the Ag nanoparticles due to the plasmon-based absorption of Ag and the dielectric confinement of the TiO_2 nanoparticle film matrix. The chromogenic properties of the Ag-TiO_2 films could be improved by simultaneous irradiation during Ag deposition with UV and blue lights to suppress the formation of anisotropic Ag particles, and nonvolatilization of a color image could be achieved by removing Ag^+ that was generated during the irradiation with a colored light [142].

Organic dyes have been widely employed as sensitizers for TiO_2 nanomaterials to improve their optical properties. Organic dyes are usually transition metal complexes with low lying excited states, such as polypyridine complexes, phthalocyanine, and metalloporphyrins. The metal centers for the dyes include Ru(II), Zn(II), Mg(II), Fe(II), and Al(III), while the ligands include nitrogen heterocyclics with a delocalized π or aromatic ring system [143–146].

4 Applications

4.1 Photocatalysis

TiO_2 is regarded as the most efficient and environmentally benign photocatalyst and has been most widely used for photodegradation of various pollutants [6,7,15,33]. TiO_2 photocatalysts can also be used to kill bacteria, as has been carried out with *E. coli* suspensions [147]. The strong oxidizing power of illuminated TiO_2 can be used to kill tumor cells in cancer treatment [148]. The photocatalytic reaction mechanisms are widely studied [6,7,15,33,149]. The principle of semiconductor photocatalytic reaction is straightforward. Upon absorption of photons with energy larger than the band gap of TiO_2, electrons are excited from the valence band to the conduction band, creating electron-hole pairs. These charge carriers migrate to the surface and react with the chemicals adsorbed on the surface to decompose these chemicals. This photodecomposition process usually involves one or more radicals or intermediate species such as ·OH, O^{2-}, H_2O_2, and O_2, which play important roles in the photocatalytic reaction mechanisms. The photocatalytic activity of a semiconductor is largely controlled by: (i) the light absorption properties, e.g., light absorption spectrum and coefficient, (ii) reduction and oxidation rates on the surface by the electron and hole, and (iii) the electron-hole recombination rate. Large surface area with constant surface density of adsorbents leads to faster surface photocatalytic reaction rates. In this sense, the larger the specific surface area, the higher the photocatalytic activity is. On the other hand, the surface is a defective site, therefore the larger the surface area, the faster the recombination. The higher the crystallinity, the fewer the bulk defects, and the higher the photocatalytic activity is. High temperature treatment usually improves the crystallinity of TiO_2 nanomaterials, which in return can induce the aggregation of small nanoparticles and decrease of the surface area. Judging from the above general conclusions, the relation between the physical properties and the photocatalytic activities is complicated. Optimal conditions are sought by taking these considerations into account and may vary from case to case [149].

4.1.1 First generation: pure TiO_2 nanomaterials

As the size of TiO_2 particle decreases, the fraction of atoms located at the surface increases with higher surface area to volume ratios, which can further enhance the catalytic activity. The increase in the bandgap energy with decreasing nanoparticle size can potentially enhance the redox potential of the valence-band holes and the conduction band electrons, allowing photoredox reactions, which might not otherwise proceed in bulk materials, to occur readily. One disadvantage of TiO_2 nanoparticles is that they can only use a small percentage of sun light for photocatalysis. Practically, there exists an optimal size for a specific photocatalytic reaction. The photocatalytic activity of TiO_2 nanoparticles on hydrogenation reactions of CH_3CCH with H_2O increased as the diameter of the TiO_2 particles decreased, especially below 10 nm [99]. The dependence of the yields on the particle size arose from the differences in the chemical reactivity and not from the physical properties of these catalysts. There was an optimal size for TiO_2 nanoparticles for maximum photocatalytic efficiency in the decomposition of chloroform [150]. For example, there was an improvement in activity when the particle size was decreased from 21 to 11 nm, but the activity decreased when the size was reduced further to 6 nm. For this particular reaction the optimum particle size was about 10 nm. In large TiO_2 nanoparticles, bulk recombination of the charge carriers was the dominant process, which could be reduced by a decrease in particle size; as the particle size was lowered below a certain limit, surface recombination processes became dominant since most of the electrons and holes were generated close to the surface and surface recombination was faster than interfacial charge carrier transfer processes [151].

4.1.2 Second generation: doped TiO_2 nanomaterials

A systematic study on the photocatalytic activity of TiO_2 nanoparticles doped with 21 transition metal elements for the oxidation of $CHCl_3$ and the reduction of CCl_4 showed that the photocatalytic activity was related to the electron configuration of the dopant ion in that dopant ions with closed electron shells had little or no effect on the activity [112,113]. Non-metal-doped TiO_2 nanomaterials have been demonstrated with improved photocatalytic activities compared to pure TiO_2 nanomaterials, especially in the visible-light region [108–110,124,125]. In the study of the decomposition of methylene blue using N-doped TiO_2 as measured by Asahi and co-workers [125], N-doped TiO_2 had much higher photocatalytic activity than pure TiO_2 in the visible-light region, while displaying lower activity in the UV-light region. A nitrogen concentration dependent performance of the photocatalytic activity of the N-doped TiO_2 was found in the visible region [125]. The concentration dependent photocatalytic activity of the N-doped TiO_2 was attributed to that the band structure of the N-doped TiO_2 with lower nitrogen concentration (< 2%) was different from that with higher concentration [122]. The significant increase in photocatalytic activity in N-doped TiO_2 nanoparticles was due to the O–Ti–N bond formation as oxynitride during the substitutional doping process [110]. Figure 5 shows a photocatalytic decomposition of methylene blue on N-doped TiO_2 nanoparticles and pure TiO_2

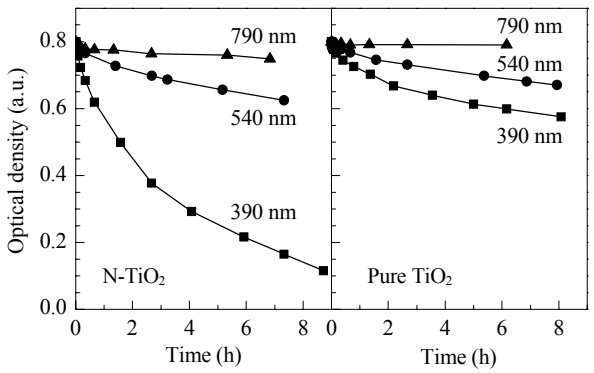


Fig. 5. Photocatalytic decomposition of methylene blue on N-doped TiO_2 nanocolloid and pure TiO_2 (Degussa P25) as monitored by the decrease in optical density at 650 nm following 790, 540, and 390 nm laser excitation after excitation of a 5 nl volume of a 2 mmol/L aqueous methylene blue solution [110].

(Degussa P25). The experiment was monitored by the decrease in optical density at 650 nm following 790, 540, and 390 nm laser excitation after excitation of a 5 nl volume of a 2 mmol aqueous methylene blue solution. N-doped TiO_2 nanocatalysts displayed a much higher photocatalytic activity from UV to visible-light region [108,110].

4.2 Photovoltaics

Photovoltaics based on TiO_2 nanocrystalline electrodes have been widely studied on the so-called dye-sensitized nanocrystalline solar cell (DSSC) [14,15]. The structure of a DSSC cell is illustrated in Fig. 6. At the heart of the system is a nanocrystalline mesoporous TiO_2 film with a monolayer of the charge transfer dye attached to its surface. The film is placed in contact with a redox electrolyte or an organic hole conductor. Photoexcitation of the dye injects an electron into the conduction band of TiO_2. The electron can be conducted to the outer circuit to drive the load and make electric power. The original state of the dye is subsequently restored by electron donation from the electrolyte, usually an organic solvent containing a redox system, such as the iodide/triiodide couple. The regeneration of the sensitizer by

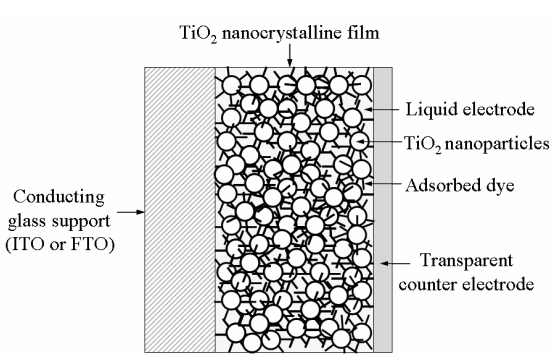


Fig. 6. Schematic illustration of the structure of a DSSC solar cell.

iodide prevents the recapture of the conduction band electron by the oxidized dye. The iodide is regenerated in turn by the reduction of triiodide at the counter-electrode, the circuit being completed via electron migration through the external load.

The structure and properties of the TiO_2 electrodes play an important role in the performance of the DSSC. The mesoporosity and nanocrystallinity of the semiconductor are important not only because of the large amount of dye that can be adsorbed on the very large surface, but also for two additional reasons: (a) they allow the semiconductor small particles to become almost totally depleted upon immersion in the electrolyte (allowing for large photovoltages), and (b) the proximity of the electrolyte to all particles makes screening of injected electrons, and thus their transport, possible [152]. Ordered mesoporous TiO_2 nanocrystalline films showed enhanced solar conversion efficiency by about 50% compared to traditional films of the same thickness made from randomly oriented anatase nanocrystals [153]. Higher efficiencies of solar cells were achieved with TiO_2 nanotube-based electrodes due to the increase in electron density in nanotube electrodes compared to P25 electrodes [154]. Nanoporous electrodes in a core-shell configuration, usually a TiO_2 core coated with Al_2O_3 [155], MgO [156], SiO_2 [157], ZrO_2 [157], or Nb_2O_5 [158], could improve the performance of dye-sensitized solar cells. Doped TiO_2 nanomaterials also show a good promise in the application of DSSCs. For the best N-doped TiO_2 electrodes, the photoinduced current due to visible light and at moderate bias increased around 200 times compared to the behavior of pure TiO_2 electrodes [159].

4.3 Solar water splitting

An enormous research effort has been dedicated to the study of the properties and applications of TiO_2 under light illumination since the discovery of photocatalytic splitting of water on a TiO_2 electrode in 1972 [5–7]. Photocatalytic splitting of water into H_2 and O_2 using TiO_2 nanomaterials continues to be a dream for clean and sustainable energy sources. The principle of water splitting using a TiO_2 photocatalyst can be summarized as follows [160]. When TiO_2 absorbs light with energy larger than the band gap, electrons and holes are generated in the conduction and valence bands, respectively. The photogenerated electrons and holes cause redox reactions. Water molecules are reduced by the electrons to form H_2 and oxidized by the holes to form O_2, leading to overall water splitting. The width of the band gap and the potentials of the conduction and valence bands are important. The bottom level of the conduction band has to be more negative than the reduction potential of H^+/H_2 (0 V vs. NHE), while the top level of the va-

lence band has to be more positive than the oxidation potential of O_2/H_2O (1.23 V). The potential of the band structure of TiO_2 is just the thermodynamical requirement. Other factors such as charge separation, mobility, and lifetime of photogenerated electrons and holes also affect the photocatalytic properties of TiO_2. These factors are strongly affected by bulk properties of the material such as crystallinity. Surface properties such as surface states, surface chemical groups, surface area, and active reaction sites are also important. The water splitting process in return affects the local pH environment and surface structures of the TiO_2 electrode [161]. A thermodynamic and kinetic study of water splitting and competitive reactions in the photoelectrochemical cell showed that the overvoltage for evolution of O must be minimized, which was on the order of 0.6 eV for *n*-TiO_2 electrodes loaded with RuO_2 [162]. Co-catalysts such as Pt and NiO are often loaded on the surface in order to introduce active sites for H_2 evolution. Addition of carbonate salts to Pt-loaded TiO_2 suspensions led to highly efficient water splitting [163].

Suitable bulk and surface properties and energy structure are demanded for photocatalysts. Figure 7 illustrates the ideal conditions for a semiconductor to perform solar photocatalytic water splitting. In this figure, it is assumed that the valence band edge (E_v) at the interface is far enough below the redox Fermi level for water oxidation ($E_F(H_2O/O_2)$) and the conduction band edge (E_c) is above the redox Fermi level for water reduction ($E_F(H_2/H_2O)$). The light splits the quasi-Fermi levels of electrons and holes so far that they exceed the energy difference for water splitting (1.23 eV) plus the additional overpotentials (η), which are assumed small for hydrogen evolution but large for oxygen evolution. The quasi-Fermi levels (E^*_F) under light at the interface between the semiconductor and the electrolyte must be at the right position for water oxidation and reduction. Including the energy losses in the electron-hole separation process and the internal resistance of the cell, a band gap (E_g) of 2.1 eV is the minimum for a semiconductor capable of solar water splitting. In reality, the band gap normally is wider, around 2.3 or 2.4 eV.

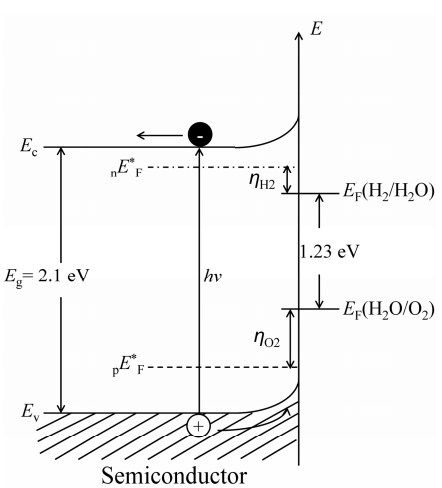


Fig. 7. Ideal conditions for a semiconductor to perform solar photocatalytic water splitting.

Pure TiO_2 cannot easily split water into H_2 and O_2 in the simple aqueous suspension system due to the fast, undesired electron-hole recombination reaction [107,164,165]. Therefore, it is important to prevent the electron-hole recombination process. A sacrificial reagent helps to control the electron-hole recombination process. Photoefficiency of the process can be improved by the addition of sacrificial reagents [164,165]. The sacrificial reagents help separation of the photoexcited electrons and holes. Various compounds such as methanol, ethanol, EDTA (an ethylenediaminetetraacetic derivative), Na_2S, Na_2SO_4, or ions such as I^-, IO_3^-, CN^-, and Fe^{3+} have been used as sacrificial reagents [164,166–168].

Highly ordered TiO_2 nanotube arrays efficiently decomposed water under UV radiation [169]. The nanotube wall thickness was a key parameter influencing the magnitude of the photoanodic response and the overall efficiency of the water-splitting reaction. For TiO_2 nanotubes with 22 nm pore diameter and 34 nm wall thickness, upon 320–400 nm illumination at an intensity of 100 mW/cm^2, hydrogen gas was generated at the power-time normalized rate of 960 μmol/(h·W) (24 ml/(h·W)) at an overall conversion efficiency of 6.8% [169,170]. When doped with carbon, $TiO_{2-x}C_x$ nanotube arrays showed more efficient water splitting under UV and visible-light illumination (> 420 nm) than pure TiO_2 nanotube arrays [115].

Water cleavage could be induced with visible light in colloidal solutions of Cr-doped TiO_2 nanoparticles deposited with ultrafine Pt or RuO_2 [171]. A pronounced synergistic effect in catalytic activity was noted when both RuO_2 and Pt were codeposited onto the particle. Jin et al. [172] found that Pt/B-doped TiO_2 was a good system for water splitting under $B_4O_7^{2-}$ environment without sacrificial electron donor reagents. Ni-doped mesoporous TiO_2 photocatalyst with 0.2% Pt accomplished hydrogen evolution at nearly 125.6 μmol/h compared to 81.2 μmol/h for TiO_2 P25 [173]. N- and B-doped TiO_2 nanomaterials have displayed higher activity than pure TiO_2 in water splitting, i.e. under visible light illumination [165,174]. C-doped TiO_2 nanocrystalline film with visible light response obtained by controlled combustion of Ti metal in a natural gas flame had a high water splitting performance with a total conversion efficiency of 11% and a maximum photoconversion efficiency of 8.35% when illuminated at 40 mW/cm^2 [116], although there were questions about its solar-to-hydrogen conversion efficiency by other researchers [175–177].

5 Summary

The tremendous effort put into TiO_2 nanomaterials has resulted in a rich database for their synthesis, properties, modifications, and applications. New properties and new applications with improved performance have been seen along with the continuing breakthroughs in the synthesis and modifications of TiO_2 nanomaterials. These new nanomaterials demonstrate the size-dependent as well as shape- and structure-dependent optical, electronic, thermal, and structural properties and have continued to be highly active in photocatalytic and photovoltaic applications, an important role in the search for renewable and clean energy technologies.

Acknowledgements

We acknowledge the financial support from the U.S. Department of Energy.

References

1 Salvador A, Pascual-Marti M C, Adell J R, Requeni A, March J G. *J Pharm Biomed Anal*, 2000, **22**: 301
2 Zallen R, Moret M P. *Solid State Commun*, 2006, **137**: 154
3 Braun J H, Baidins A, Marganski R E. *Prog Org Coat*, 1992, **20**: 105
4 Reck E, Richards M. *Pigment Resin Technol*, 1999, **28**: 149
5 Fujishima A, Honda K. *Nature*, 1972, **238**: 37
6 Fujishima A, Rao T N, Tryk D A. *J Photochem Photobiol C*, 2000, **1**: 1
7 Tryk D A, Fujishima A, Honda K. *Electrochim Acta*, 2000, **45**: 2363
8 Burda C, Chen X B, Narayanan R, El-Sayed M A. *Chem Rev*, 2005, **105**: 1025
9 Chen X B, Lou Y B, Dayal S, Qiu X F, Krolicki R, Burda C. *J Nanosci Nanotechnol*, 2005, **5**: 1408
10 Chen X B, Mao S S. *Chem Rev*, 2007, **107**: 2891
11 Chen X B, Mao S S. *J Nanosci Nanotechnol*, 2006, **6**: 906
12 Cozzoli P D, Pellegrino T, Manna L. *Chem Soc Rev*, 2006, **35**: 1195
13 Millis A, Hunte S L. *J Photochem Photobiol A*, 1997, **108**: 1
14 Grätzel M. *Prog Photovolt*, 2000, **8**: 171
15 Grätzel M. *Nature*, 2001, **414**: 338
16 Lan Y, Gao X D, Zhu H Y, Zheng Z F, Yan T Y, Wu F, Ringer S P, Song D Y. *Adv Funct Mater*, 2005, **15**: 1310
17 Holland B T, Blanford C F, Stein A. *Science*, 1998, **281**: 538
18 Holland B T, Blanford C F, Do T, Stein A. *Chem Mater*, 1999, **11**: 795
19 Mor G K, Varghese O K, Paulose M, Grimes C A. *Sens Lett*, 2003, **1**: 42
20 Hwang D K, Moon J H, Shul Y G, Jung K T, Kim D H, Lee D W. *J Sol-Gel Sci Technol*, 2003, **26**: 783
21 Meilert K T, Laub D, Kiwi J. *J Mol Catal A*, 2005, **237**: 101
22 Pfaff G, Reynders P. *Chem Rev*, 1999, **99**: 1963
23 Hagfeldt A, Grätzel M. *Chem Rev*, 1995, **95**: 49
24 Linsebigler A L, Lu G Q, Yates J T. *Chem Rev*, 1995, **95**: 735
25 Bessekhouad Y, Robert D, Weber J V. *J Photochem Photobiol A*, 2003, **157**: 47
26 Oskam G, Nellore A, Penn R L, Searson P C. *J Phys Chem B*, 2003, **107**: 1734
27 Sugimoto T. *Adv Colloid Interface Sci*, 1987, **28**: 65
28 Niederberger M, Bartl M H, Stucky G D. *Chem Mater*, 2002, **14**: 4364
29 Parala H, Devi A, Bhakta R, Fischer R A. *J Mater Chem*, 2002, **12**: 1625
30 Tang J, Redl F, Zhu Y M, Siegrist T, Brus L E, Steigerwald M L. *Nano Lett*, 2005, **5**: 543
31 Arnal P, Corriu R J P, Leclercq D, Mutin P H, Vioux A. *J Mater Chem*, 1996, **6**: 1925
32 Arnal P, Corriu R J P, Leclercq D, Mutin P H, Vioux A. *Chem Mater*, 1997, **9**: 694
33 Hay J N, Raval H M. *J Sol-Gel Sci Technol*, 1998, **13**: 109
34 Hay J N, Raval H M. *Chem Mater*, 2001, **13**: 3396
35 Lafond V, Mutin P H, Vioux A. *Chem Mater*, 2004, **16**: 5380
36 Trentler T J, Denler T E, Bertone J F, Agrawal A, Colvin V L. *J Am Chem Soc*, 1999, **121**: 1613
37 Hong S S, Lee M S, Park S S, Lee G D. *Catal Today*, 2003, **87**: 99
38 Kim K D, Kim S H, Kim H T. *Colloids Surf A*, 2005, **254**: 99
39 Li G L, Wang G H. *Nanostruct Mater*, 1999, **11**: 663
40 Lin J, Lin Y, Liu P, Meziani M J, Allard L F, Sun Y P. *J Am Chem Soc*, 2002, **124**: 11514
41 Yu J C, Yu J G, Ho W, Zhang L Z. *Chem Commun*, 2001: 1942
42 Zhang D B, Qi L M, Ma J M, Cheng H M. *J Mater Chem*, 2002, **12**: 3677
43 Scolan E, Sanchez C. *Chem Mater*, 1998, **10**: 3217
44 Cozzoli P D, Comparelli R, Fanizza E, Curri M L, Agostiano A. *Mater Sci Eng C*, 2003, **23**: 707
45 Cozzoli P D, Fanizza E, Curri M L, Laub D, Agostiano A. *Chem Commun*, 2005: 942
46 Cozzoli P D, Kornowski A, Weller H. *J Am Chem Soc*, 2003, **125**: 14539
47 Cozzoli P D, Comparelli R, Fanizza E, Curri M L, Agostiano A, Laub D. *J Am Chem Soc*, 2004, **126**: 3868
48 Joo J, Kwon S G, Yu T, Cho M, Lee J, Yoon J, Hyeon T. *J Phys Chem B*, 2005, **109**: 15297
49 Jun Y W, Casula M F, Sim J H, Kim S Y, Cheon J, Alivisatos A P. *J Am Chem Soc*, 2003, **125**: 15981
50 Zhang Z H, Zhong X H, Liu S H, Li D F, Han M Y. *Angew Chem, Int Ed*, 2005, **44**: 3466
51 Miao L, Tanemura S, Toh S, Kaneko K, Tanemura M. *J Crystal Growth*, 2004, **264**: 246
52 Lin Y, Wu G S, Yuan X Y, Xie T, Zhang L D. *J Phys-Cond Mater*, 2003, **15**: 2917
53 Chen Y S, Crittenden J C, Hackney S, Sutter L, Hand D W. *Environ Sci Technol*, 2005, **39**: 1201
54 Jung J H, Kobayashi H, van Bommel K J C, Shinkai S, Shimizu T. *Chem Mater*, 2002, **14**: 1445

55 Cot F, Larbot A, Nabias G, Cot L. *J Eur Ceram Soc*, 1998, **18**: 2175
56 Yang J, Mei S, Ferreira J M F. *J Am Ceram So*c, 2000, **83**: 1361
57 Feng X J, Zhai J, Jiang L. *Angew Chem*, *Int Ed*, 2005, **44**: 5115
58 Yang S W, Gao L. *Chem Lett*, 2005, **34**: 1044
59 Yang S W, Gao L. *Chem Lett*, 2005, **34**: 964
60 Bavykin D V, Gordeev S N, Moskalenko A V, Lapkin A A, Walsh F C. *J Phys Chem B*, 2005, **109**: 8565
61 Bavykin D V, Lapkin A A, Plucinski P K, Friedrich J M, Walsh F C. *J Catal*, 2005, **235**: 10
62 Kasuga T, Hiramatsu M, Hoson A, Sekino T, Niihara K. *Langmuir*, 1998, **14**: 3160
63 Kasuga T, Hiramatsu M, Hoson A, Sekino T, Niihara K. *Adv Mater*, 1999, **11**: 1307
64 Li X L, Peng Q, Yi J X, Wang X, Li Y D. *Chem-Eur J*, 2006, **12**: 2383
65 Wang X, Zhuang J, Peng Q, Li Y D. *Nature*, 2005, **437**: 121
66 Kim C S, Moon B K, Park J H, Choi B C, Seo H J. *J Cryst Growth*, 2003, **257**: 309
67 Kim C S, Moon B K, Park J H, Chung S T, Son S M. *J Cryst Growth*, 2003, **254**: 405
68 Gong D, Grimes C A, Varghese O K, Hu W C, Singh R S, Chen Z, Dickey E C. *J Mater Res*, 2001, **16**: 3331
69 Mor G K, Varghese O K, Paulose M, Mukherjee N, Grimes C A. *J Mater Res*, 2003, **18**: 2588
70 Varghese O K, Gong D W, Paulose M, Grimes C A, Dickey E C. *J Mater Res*, 2003, **18**: 156
71 Varghese O K, Mor G K, Grimes C A, Paulose M, Mukherjee N. *J Nanosci Nanotechnol*, 2004, **4**: 733
72 Varghese O K, Paulose M, Shankar K, Mor G K, Grimes C A. *J Nanosci Nanotechnol*, 2005, **5**: 1158
73 Chen X B, Schriver M, Suen T, Mao S S. *Thin Solid Films*, 2007, **515**: 8511
74 Wu J M, Hayakawa S, Tsuru K, Osaka A. *Scripta Mater*, 2002, **46**: 101
75 Wu J M, Zhang T W, Zeng Y W, Hayakawa S, Tsuru K, Osaka A. *Langmuir*, 2005, **21**: 6995
76 Peng X S, Chen A C. *J Mater Chem*, 2004, **14**: 2542
77 Seifried S, Winterer M, Hahn H. *Chem Vap Deposition*, 2000, **6**: 239
78 Wu J J, Yu C C. *J Phys Chem B*, 2004, **108**: 3377
79 Xiang B, Zhang Y, Wang Z, Luo X H, Zhu Y W, Zhang H Z, Yu D P. *J Phys D*, 2005, **38**: 1152
80 Wu J M, Shih H C, Wu W T. *Chem Phys Lett*, 2005, **413**: 490
81 Wu J M, Shih H C, Wu W T, Tseng Y K, Chen I C. *J Crystal Growth*, 2005, **281**: 384
82 Blesic M D, Saponjic Z V, Nedeljkovic J M, Uskokovic D P. *Mater Lett*, 2002, **54**: 298
83 Guo W L, Lin Z M, Wang X K, Song G Z. *Microelectron Eng*, 2003, **66**: 95
84 Yu J C, Zhang L Z, Yu J G. *Chem Mater*, 2002, **14**: 4647
85 Zhu Y, Li H, Koltypin Y, Hacohen Y R, Gedanken A. *Chem Commun*, 2001: 2616
86 Corradi A B, Bondioli F, Focher B, Ferrari A M, Grippo C, Mariani E, Villa C. *J Am Ceram Soc*, 2005, **88**: 2639
87 Gressel-Michel E, Chaumont D, Stuerga D. *J Colloid Interface Sci*, 2005, **285**: 674
88 Wu X, Jiang Q Z, Ma Z F, Fu M, Shangguan W F. *Solid State Commun*, 2005, **136**: 513
89 Zhang H Z, Banfield J F. *J Mater Chem*, 1998, **8**: 2073
90 Zhang H Z, Banfield J F. *J Phys Chem B*, 2000, **104**: 3481
91 Hwu Y, Yao Y D, Cheng N F, Tung C Y, Lin H M. *Nanostruct Mater*, 1997, **9**: 355
92 Gribb A A, Banfield J F. *Am Mineral*, 1997, **82**: 717
93 Ye X S, Sha J, Jiao Z K, Zhang L D. *Nanostruct Mater*, 1998, **8**: 919
94 Barnard A S, Zapol P. *Phys Rev B*, 2004, **70**: 235403
95 Barnard A S, Zapol P. *J Phys Chem B*, 2004, **108**: 18435
96 Barnard A S, Zapol P, Curtiss L A. *J Chem Theory Comput*, 2005, **1**: 107
97 Brydson R, Williams B G, Engel W, Sauer H, Zeitler E, Thomas J M. *Solid State Commun*, 1987, **64**: 609
98 Zimmermann R, Steiner P, Claessen R, Reinert F, Hufner S. *J Electron Spectrosc Relat Phenom*, 1998, **96**: 179
99 Anpo M, Shima T, Kodama S, Kubokawa Y. *J Phys Chem*, 1987, **91**: 4305
100 Kavan L, Stoto T, Graetzel M, Fitzmaurice D, Shklover V. *J Phys Chem*, 1993, **97**: 9493
101 Henglein A. *Chem Rev*, 1989, **89**: 1861
102 Serpone N, Lawless D, Khairutdinov R, Pelizzetti E. *J Phys Chem*, 1995, **99**: 16655
103 Li Y, White T J, Lim S H. *J Solid State Chem*, 2004, **177**: 1372
104 Reddy K M, Reddy C V G, Manorama S V. *J Solid State Chem*, 2001, **158**: 180
105 Braginsky L, Shklover V. *Eur Phys J D*, 1999, **9**: 627
106 Sakai N, Ebina Y, Takada K, Sasaki T. *J Am Chem Soc*, 2004, **126**: 5851
107 Sato H, Ono K, Sasaki T, Yamagishi A. *J Phys Chem B*, 2003, **107**: 9824
108 Burda C, Lou Y B, Chen X B, Samia A C S, Stout J, Gole J L. *Nano Lett*, 2003, **3**: 1049
109 Chen X B, Burda C. *J Phys Chem B*, 2004, **108**: 15446
110 Chen X B, Lou Y B, Samia A C S, Burda C, Gole J L. *Adv Funct Mater*, 2005, **15**: 41
111 Bessekhouad Y, Robert D, Weber J V, Chaoui N. *J Photochem Photobiol A*, 2004, **167**: 49
112 Choi W, Termin A, Hoffmann M R. *J Phys Chem*, 1994, **98**: 13669
113 Choi W, Termin A, Hoffmann M R. *Angew Chem*, *Int Ed*, 1994, **33**: 1091
114 Choi Y, Umebayashi T, Yoshikawa M. *J Mater Sci*, 2004, **39**: 1837
115 Park J H, Kim S, Bard A J. *Nano Lett*, 2006, **6**: 24
116 Khan S U M, Al-Shahry M, Ingler W B Jr. *Science*, 2002, **297**: 2243
117 Chen X B, Lou Y B, Burda C. *Int J Nanotechnol*, 2004, **1**: 105
118 Gole J L, Stout J D, Burda C, Lou Y B, Chen X B. *J Phys Chem B*, 2004, **108**: 1230

119 Liu Y, Chen X, Li J, Burda C. *Chemosphere*, 2005, **61**: 11
120 Prokes S M, Gole J L, Chen X, Burda C, Carlos W E. *Adv Funct Mater*, 2005, **15**: 161
121 Sakthivel S, Kisch H. *Chem Phys Chem*, 2003, **4**: 487
122 Irie H, Watanabe Y, Hashimoto K. *J Phys Chem B*, 2003, **107**: 5483
123 Chen S F, Chen L, Gao S, Cao G Y. *Chem Phys Lett*, 2005, **413**: 404
124 Diwald O, Thompson T L, Zubkov T, Goralski E G, Walck S D, Yates J T Jr. *J Phys Chem B*, 2004, **108**: 6004
125 Asahi R, Morikawa T, Ohwaki T, Aoki K, Taga Y. *Science*, 2001, **293**: 269
126 Diwald O, Thompson T L, Goralski E G, Walck S D, Yates J T Jr. *J Phys Chem B*, 2004, **108**: 52
127 Ohno T, Akiyoshi M, Umebayashi T, Asai K, Mitsui T, Matsumura M. *Appl Catal A*, 2004, **265**: 115
128 Umebayashi T, Yamaki T, Itoh H, Asai K. *Appl Phys Lett*, 2002, **81**: 454
129 Yu J G, Yu J C, Cheng B, Hark S K, Iu K. *J Solid State Chem*, 2003, **174**: 372
130 Subbarao S N, Yun Y H, Kershaw R, Dwight K, Wold A. *Mater Res Bull*, 1978, **13**: 1461
131 Li D, Haneda H, Labhsetwar N K, Hishita S, Ohashi N. *Chem Phys Lett*, 2005, **401**: 579
132 Luo H M, Takata T, Lee Y, Zhao J F, Domen K, Yan Y S. *Chem Mater*, 2004, **16**: 846
133 Luo Z H, Gao Q H. *J Photochem Photobiol A*, 1992, **63**: 367
134 Wang Y Q, Cheng H M, Hao Y Z, Ma J M, Li W H, Cai S M. *J Mater Sci*, 1999, **34**: 3721
135 Chen X B, Burda C. *J Am Chem Soc*, 2008, **130**: 5018
136 Chen X B, Glans P A, Qiu X F, Dayal S, Jennings W D, Smith K E, Burda C, Guo J. *J Electron Spectrosc Relat Phenom*, 2008, **162**: 67
137 Lin Z S, Orlov A, Lambert R M, Payne M C. *J Phys Chem B*, 2005, **109**: 20948
138 Fitzmaurice D, Frei H, Rabani J. *J Phys Chem*, 1995, **99**: 9176
139 Hoyer P, Koenenkamp R. *Appl Phys Lett*, 1995, **66**: 349
140 Vogel R, Hoyer P, Weller H. *J Phys Chem*, 1994, **98**: 3183
141 Ohko Y, Tatsuma T, Fujii T, Naoi K, Niwa C, Kubota Y, Fujishima A. *Nature Mater*, 2003, **2**: 29
142 Naoi K, Ohko Y, Tatsuma T. *J Am Chem Soc*, 2004, **126**: 3664
143 Blackbourn R L, Johnson C S, Hupp J T. *J Am Chem Soc*, 1991, **113**: 1060
144 Meyer G J. *Inorg Chem*, 2005, **44**: 6852
145 Rehm J M, McLendon G L, Nagasawa Y, Yoshihara K, Moser J, Gratzel M. *J Phys Chem*, 1996, **100**: 9577
146 van de Lagemaat J, Frank A J. *J Phys Chem B*, 2000, **104**: 4292
147 Kikuchi Y, Sunada K, Iyoda T, Hashimoto K, Fujishima A. *J Photochem Photobiol A*, 1997, **106**: 51
148 Sakai H, Baba R, Hashimoto K, Kubota Y, Fujishima A. *Chem Lett*, 1995, **24**: 185
149 Beydoun D, Amal R, Low G, McEvoy S. *J Nanoparticle Res*, 1999, **1**: 439
150 Wang C C, Zhang Z B, Ying J Y. *Nanostruct Mater*, 1997, **9**: 583
151 Zhang Z B, Wang C C, Zakaria R, Ying J Y. *J Phys Chem B*, 1998, **102**: 10871
152 Cahen D, Hodes G, Grätzel M, Guillemoles J F, Riess I. *J Phys Chem B*, 2000, **104**: 2053
153 Zukalova M, Zukal A, Kavan L, Nazeeruddin M K, Liska P, Graetzel M. *Nano Lett*, 2005, **5**: 1789
154 Ohsaki Y, Masaki N, Kitamura T, Wada Y, Okamoto T, Sekino T, Niihara K, Yanagida S. *Phys Chem Chem Phys*, 2005, **7**: 4157
155 Fabregat-Santiago F, Garcia-Canadas J, Palomares E, Clifford J N, Haque S A, Durrant J R, Garcia-Belmonte G, Bisquert J. *J Appl Phys*, 2004, **96**: 6903
156 Kumara G R A, Okuya M, Murakami K, Kaneko S, Jayaweera V V, Tennakone K. *J Photochem Photobiol A*, 2004, **164**: 183
157 Palomares E, Clifford J N, Haque S A, Lutz T, Durrant J R. *J Am Chem Soc*, 2003, **125**: 475
158 Chen S G, Chappel S, Diamant Y, Zaban A. *Chem Mater*, 2001, **13**: 4629
159 Lindgren T, Mwabora J M, Avendano E, Jonsson J, Hoel A, Granqvist C G, Lindquist S E. *J Phys Chem B*, 2003, **107**: 5709
160 Kudo A. *Catal Surv Asia*, 2003, **7**: 31
161 Tafalla D, Salvador P. *J Electroanal Chem Interfacial Electrochem*, 1989, **270**: 285
162 Salvador P. *New J Chem*, 1988, **12**: 35
163 Sayama K, Arakawa H. *J Chem Soc*, *Faraday Trans*, 1997, **93**: 1647
164 Abe R, Sayama K, Arakawa H. *Chem Phys Lett*, 2003, **371**: 360
165 Moon S C, Mametsuka H, Tabata S, Suzuki E. *Catal Today*, 2000, **58**: 125
166 Abe R, Sayama K, Domen K, Arakawa H. *Chem Phys Lett*, 2001, **344**: 339
167 Abe R, Sayama K, Sugihara H. *J Phys Chem B*, 2005, **109**: 16052
168 Galinska A, Walendziewski J. *Energy Fuels*, 2005, **19**: 1143
169 Mor G K, Shankar K, Paulose M, Varghese O K, Grimes C A. *Nano Lett*, 2005, **5**: 191
170 Mor G K, Varghese O K, Paulose M, Shankar K, Grimes C A. *Mater Photovolt*, 2005, **836**: 29
171 Borgarello E, Kiwi J, Graetzel M, Pelizzetti E, Visca M. *J Am Chem Soc*, 1982, **104**: 2996
172 Jin Z L, Lu G X. *Energy Fuels*, 2005, **19**: 1126
173 Jing D W, Zhang Y J, Guo L J. *Chem Phys Lett*, 2005, **415**: 74
174 Torres G R, Lindgren T, Lu J, Granqvist C G, Lindquist S E. *J Phys Chem B*, 2004, **108**: 5995
175 Fujishima A. *Science*, 2003, **301**: 1673
176 Hägglund C, Grätzel M, Kasemo B. *Science*, 2003, **301**: 1673
177 Lackner K S. *Science*, 2003, **301**: 1673